Supporting information to: Evaluating post-perovskite as a cause of D″ anisotropy in regions of palaeosubduction

Andy Nowacki*, Andrew M. Walker, James Wookey and J.-Michael Kendall

School of Earth Sciences, University of Bristol, Bristol, UK. (*andy.nowacki@bristol.ac.uk)

Texture calculations with MgO

In order to assess the impact of the inclusion of MgO in our texture calculations, we compared a simple case of one layer of constants with no topography on the pv–ppv transition, as for Walker et al. (2011).

The first set of constants are made with the same set of plasticities as the rest of this work (top panel, Figure S5). For the second set (middle panel), a random mixture of 80% ppv and 20% MgO was used, using the slip system activities for MgO used by Wenk et al. (2011) and the single-crystal elastic constants of MgO of Mao et al. (2010). There is no experimental constraint on the relative strengths of the slip systems between ppv and MgO, so to maximise the texture development in MgO, its weakest slip system was set to be half as strong as that in ppv.

The bottom panel shows the case where two separate VPSC calculations were made, using pure ppv and MgO, and the resulting constants from the two runs mixed in the same ratio as before to produce the final set of constants. This is in an effort to represent the case where the two phases are completely segregated.

The results show that there is little difference in the pattern of anisotropy exhibited, apart from the overall strength. The MgO-absent case has the largest overall anisotropy, whilst the unmixed case has the lowest. The overall difference is not major, though, being similar to the proportion of the mixture which is MgO (20%).

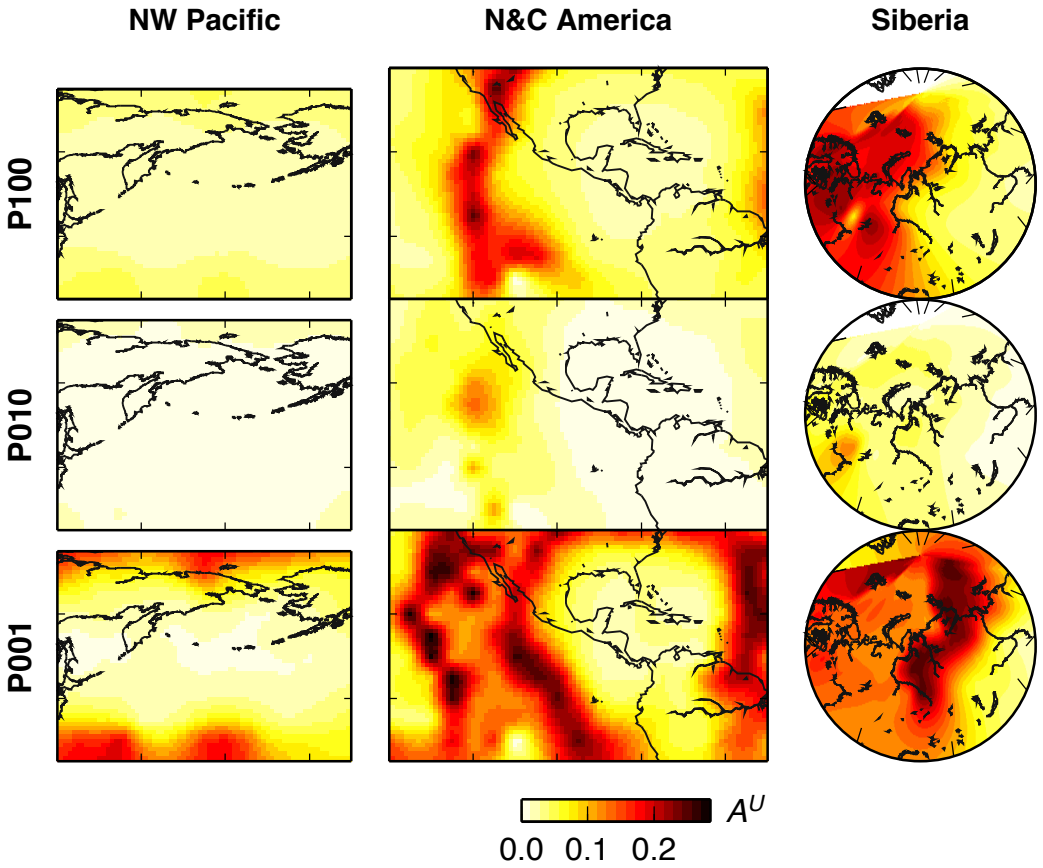

Figure S1. Strength of anisotropy of elastic constants for each plasticity model used in the shear wave splitting calculations at radius 3555 km (75 km above the CMB). Shown are the values of A^U, the universal anisotropy index (Ranganathan & Ostoja-Starzewski, 2008), for the aggregate elasticity tensors, evaluated each 5° in latitude and longitude. The three plasticity cases, P100, P010 and P001 are shown for the three regions investigated here (left: Northwest Pacific; middle: Americas; right: Siberia). Black squares show 5° blocks outside of the ppv stability field, hence no texturing is assumed. White area at top of Siberia plot show that no constants were evaluated outside the coloured area.

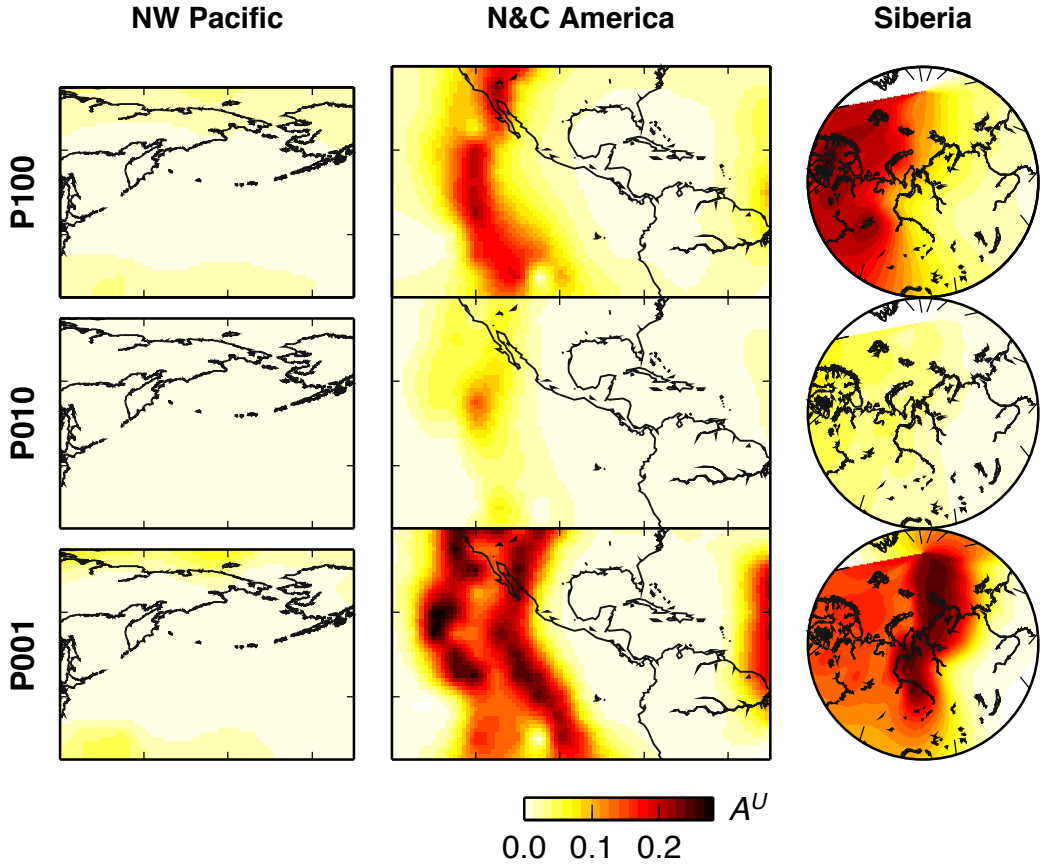

Figure S2. Strength of anisotropy of elastic constants for each plasticity model used in the shear wave splitting calculations at radius 3605 km (125 km above the CMB). Same as for Figure S1.

Table S1. Event-receiver geometries for shear wave splitting measurements we compare to predictions from the texture model. 'Events' and 'receivers' are average (usually median) locations for average (NW Pacific) or stacked measurements of splitting.

Label	Event lat (°N)	Event lon (°E)	Depth (km)	Receiver lat	Receiver lon	ϕ' (°)	$\Delta(\phi')$ (°)	δt (s)	$\Delta(\delta t)$ (s)
				NW Pacific					
P	23.3	142.3	324.5	61.9	−117.1	49	7	2.1	0.4
				North and Central America					
W1	19.3	−155.0	9	40.7	−86.2	−80	6	1.10	0.04
W2	10.7	−86.5	47	56.3	−151.1	77	10	1.25	0.03
S1	−7.0	−107.7	10	49.3	−74.4	−42	4	1.68	0.04
S2	−8.1	−71.3	645	40.4	−116.6	−84	3	0.90	0.01
E1	−8.1	−71.2	645	53.6	−79.2	83	8	1.28	0.10
E2	7.3	−34.9	9	40.1	−106.5	45	7	1.78	0.02
				Siberia					
Sib1	36.5	70.84	183	64.5	−111.0	87	4	2.70	0.18
Sib2	45.2	148.5	130	49.5	8.79	35	11	1.45	0.16

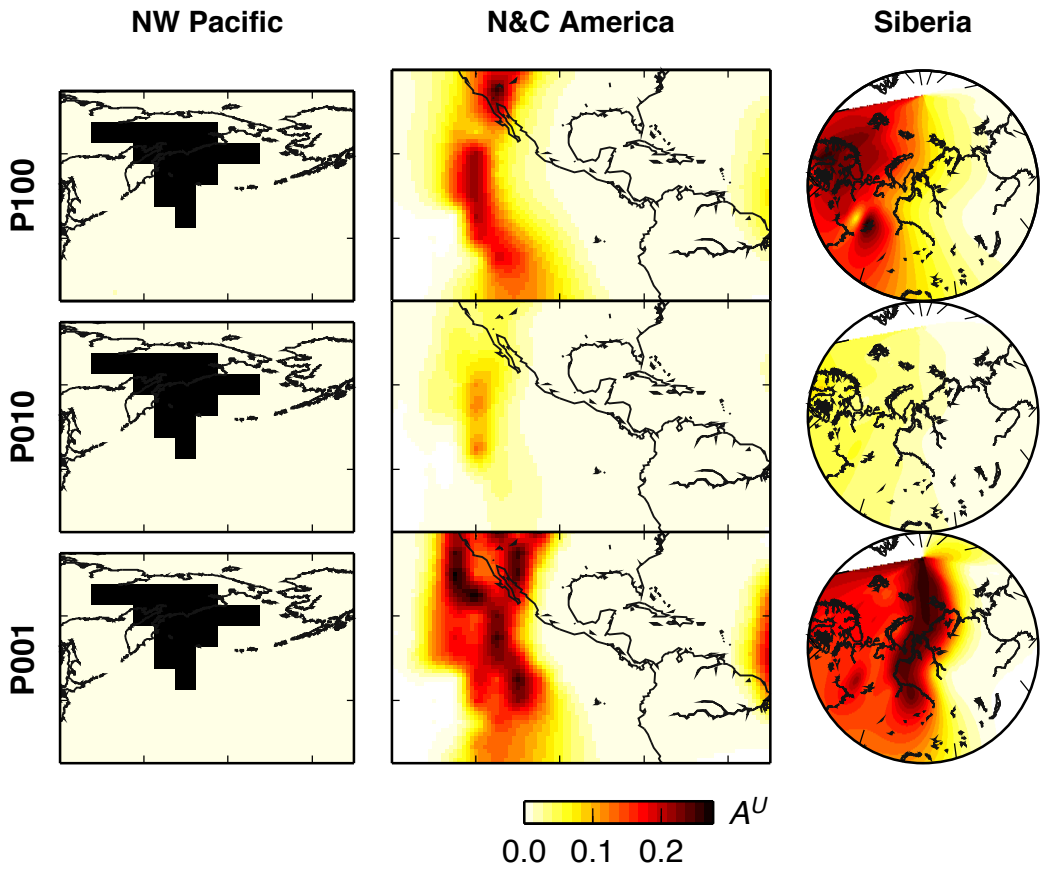

Figure S3. Strength of anisotropy of elastic constants for each plasticity model used in the shear wave splitting calculations at radius 3655 km (175 km above the CMB). Same as for Figure S1. Note that by comparison with the figure in the main text, and observing the instability region of ppv in NW Pacific, a double-crossing of the pv–ppv phase boundary has occurred in this region.

Table S2. Synthetic shear wave splitting predicted from each plasticity model for each raypath. Paths W1 for P100 and W2 for the P001 model are excluded.

Model	Path	ϕ' / °	$\Delta(\phi')$ / °	δt / s	$\Delta(\delta t)$ / s	$\langle\delta t\rangle$ / s [a]
	E1	−66.0	1.0	3.98	0.90	
	E2	84.0	1.5	5.47	0.26	
	S1	62.0	3.8	1.95	0.06	
	S2	−11.0	4.0	2.10	0.09	
P100	W1	–	–	–	–	7.5
	W2	−84.0	7.2	5.78	0.32	
	P	−63.0	1.5	4.50	0.17	
	Sib1	35.0	1.2	23.00	0.31	
	Sib2	33.0	2.0	13.25	0.50	
	E1	−51.0	5.5	1.43	0.30	
	E2	−14.0	2.2	1.88	0.15	
	S1	−14.0	9.2	1.05	0.23	
	S2	−61.0	23.2	2.17	2.98	
P010	W1	64.0	1.0	3.23	0.45	3.2
	W2	84.0	1.5	3.67	0.04	
	P	79.0	20.8	0.70	0.63	
	Sib1	31.0	9.2	5.00	0.56	
	Sib2	17.0	4.5	9.75	1.81	
	E1	78.0	9.8	2.17	0.47	
	E2	73.0	1.5	3.67	0.13	
	S1	61.0	2.0	3.15	0.06	
	S2	33.0	23.8	1.65	2.96	
P001	W1	−73.0	10.0	2.10	0.41	3.8
	W2	–	–	–	–	
	P	28.0	4.0	2.20	0.33	
	Sib1	21.0	3.5	10.75	0.31	
	Sib2	−55.0	10.2	5.25	0.94	

[a] Mean δt given for each plasticity model.

Table S3. Misfit of synthetic shear wave splitting fast orientations compared to previous observations for each plasticity model.

Model	$\langle\delta t\rangle$ / s [a]	χ_c^2	1σ bounds [b]	2σ bounds [b]
P100	7.5	108	(48.8, 97.4)	(24.5, 121.7)
P010	3.2	46	(48.0, 91.2)	(26.4, 112.8)
P001	3.8	109	(52.5, 101.9)	(27.8, 126.6)

[a] Mean δt for all paths.

[b] One- and two-standard deviation range of χ_c^2 values for a sample of 500,000 random orientations.

Figure S4. Examples of synthetic split waveforms and minimum-eigenvalue surfaces. An example is given for each of the three plasticity models. Top panels show waveform before (left) and after (right) application of optimal apparent splitting operator when rotated to the optimal fast orientation. Middle panels show particle motion before and after correction with best splitting. Bottom panels show λ_2 surfaces for analysis, with the 95% confidence contour shown as thick line. Note W2 for P001 is excluded from further analysis because no single apparent splitting operator can recover adequately linear particle motion.

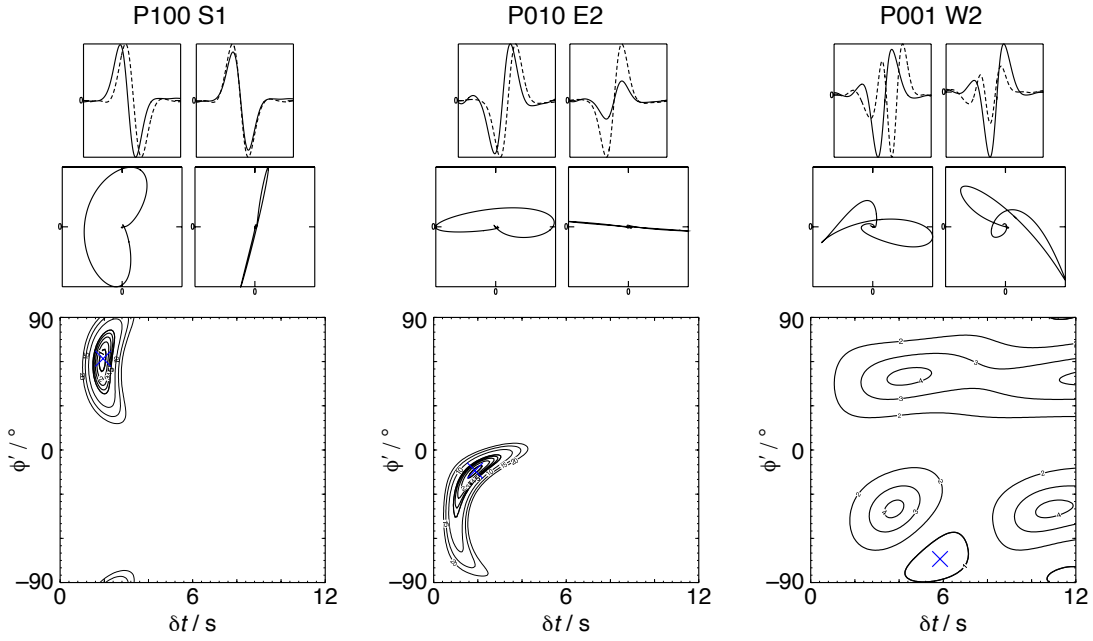

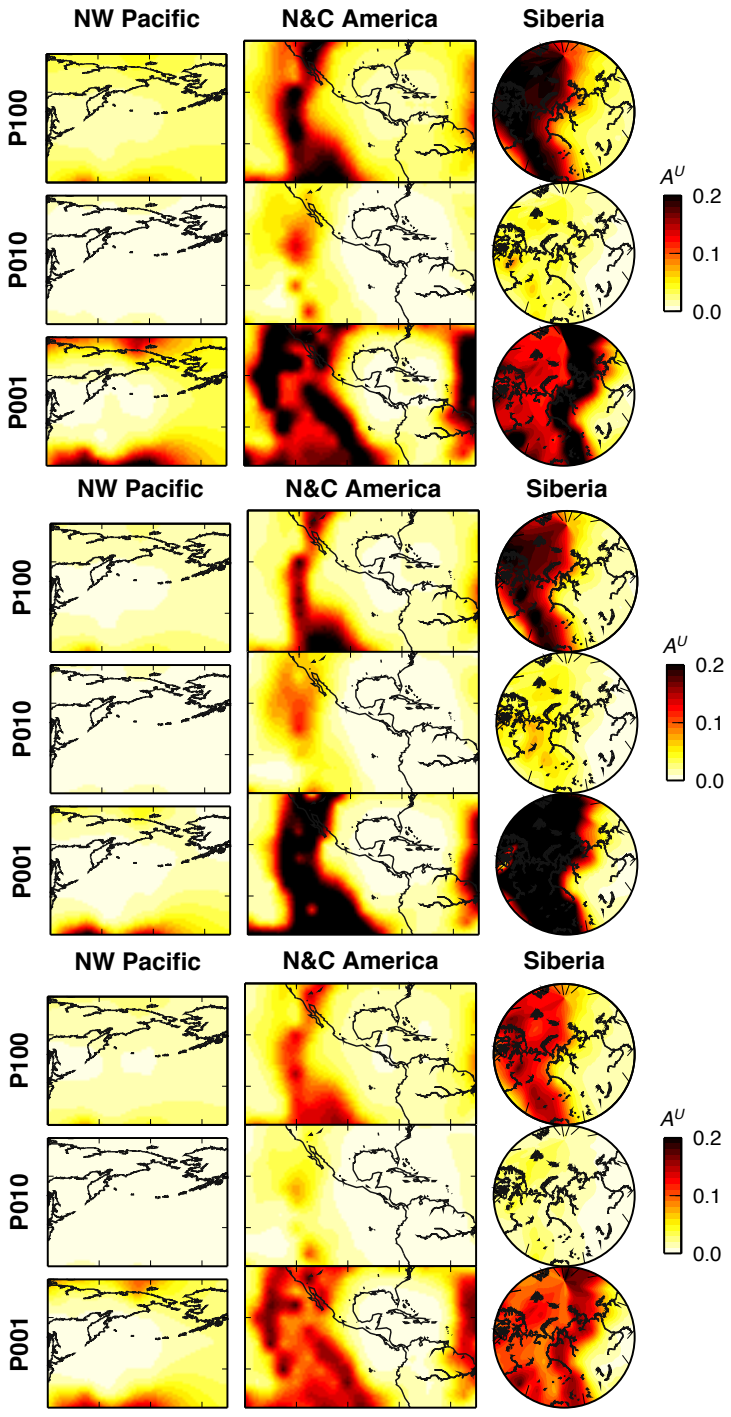

Figure S5. Strength of anisotropy for elastic constants without MgO (top), with MgO mixed with ppv (middle) and with MgO and ppv forming separated aggregates. Average and peak values of A^U are highest for the case without MgO, then for the mixture, then for the separated phase calculations.

References

Mao, W. L., Meng, Y., & Mao, H., 2010. Elastic anisotropy of ferromagnesian post-perovskite in Earth's D″ layer, *Phys. Earth Planet. Inter.*, **180**(3-4), 203–208, doi:10.1016/j.pepi.2009.10.013.

Ranganathan, S. I. & Ostoja-Starzewski, M., 2008. Universal elastic anisotropy index, *Phys. Rev. Lett.*, **101**(5), 055504, doi:10.1103/PhysRevLett.101.055504.

Walker, A. M., Forte, A. M., Wookey, J., Nowacki, A., & Kendall, J. M., 2011. Elastic anisotropy of D″ predicted from global models of mantle flow, *Geochem Geophy Geosy*, **12**(10), Q10006, doi:10.1029/2011GC003732.

Wenk, H.-R., Cottaar, S., Tomé, C. N., McNamara, A. K., & Romanowicz, B., 2011. Deformation in the lowermost mantle: From polycrystal plasticity to seismic anisotropy, *Earth Planet Sci Lett*, **306**(1-2), 33–45, doi:10.1016/j.epsl.2011.03.021.